The Astrophysical Journal, 718:133–147, 2010 July 20 doi:10.1088/0004-637X/718/1/133

THE *XMM* CLUSTER SURVEY: ACTIVE GALACTIC NUCLEI AND STARBURST GALAXIES IN XMMXCS J2215.9−1738 AT $z = 1.46$

Matt Hilton[1], Ed Lloyd-Davies[2], S. Adam Stanford[3,4], John P. Stott[5], Chris A. Collins[5], A. Kathy Romer[2], Mark Hosmer[2], Ben Hoyle[6], Scott T. Kay[7], Andrew R. Liddle[2], Nicola Mehrtens[2], Christopher J. Miller[8], Martin Sahlén[9], and Pedro T. P. Viana[10,11]

[1] Astrophysics & Cosmology Research Unit, School of Mathematical Sciences, University of KwaZulu-Natal, Private Bag X54001, Durban 4000, South Africa; hiltonm@ukzn.ac.za

[2] Astronomy Centre, University of Sussex, Falmer, Brighton, BN1 9QH, UK

[3] University of California, Davis, CA 95616, USA

[4] Institute of Geophysics and Planetary Physics, Lawrence Livermore National Laboratory, Livermore, CA 94551, USA

[5] Astrophysics Research Institute, Liverpool John Moores University, Twelve Quays House, Egerton Wharf, Birkenhead, CH41 1LD, UK

[6] Institut de Ciències del Cosmos (ICCUB), Departmento de Física, Martí i Franqués 1, 08034 Barcelona, Spain

[7] University of Manchester, Jodrell Bank Observatory, Macclesfield, Cheshire, SK11 9DL, UK

[8] Astronomy Department, University of Michigan, Ann Arbor, MI 48109, USA

[9] The Oskar Klein Centre for Cosmoparticle Physics, Department of Physics, Stockholm University, AlbaNova, SE-106 91 Stockholm, Sweden

[10] Departamento de Física e Astronomia da Faculdade de Ciências da Universidade do Porto, Rua do Campo Alegre 687, 4169-007 Porto, Portugal

[11] Centro de Astrofísica da Universidade do Porto, Rua das Estrelas, 4150-762 Porto, Portugal

Received 2010 March 17; accepted 2010 May 24; published 2010 June 28

ABSTRACT

We use *Chandra* X-ray and *Spitzer* infrared (IR) observations to explore the active galactic nucleus (AGN) and starburst populations of XMMXCS J2215.9−1738 at $z = 1.46$, one of the most distant spectroscopically confirmed galaxy clusters known. The high-resolution X-ray imaging reveals that the cluster emission is contaminated by point sources that were not resolved in *XMM-Newton* observations of the system, and have the effect of hardening the spectrum, leading to the previously reported temperature for this system being overestimated. From a joint spectroscopic analysis of the *Chandra* and *XMM-Newton* data, the cluster is found to have temperature $T = 4.1^{+0.6}_{-0.9}$ keV and luminosity $L_X = (2.92^{+0.24}_{-0.35}) \times 10^{44}$ erg s^{-1}, extrapolated to a radius of 2 Mpc. As a result of this revised analysis, the cluster is found to lie on the σ_v–T relation, but the cluster remains less luminous than would be expected from self-similar evolution of the local L_X–T relation. Two of the newly discovered X-ray AGNs are cluster members, while a third object, which is also a prominent 24 μm source, is found to have properties consistent with it being a high-redshift, highly obscured object in the background. We find a total of eight $>5\sigma$ 24 μm sources associated with cluster members (four spectroscopically confirmed and four selected using photometric redshifts) and one additional 24 μm source with two possible optical/near-IR counterparts that may be associated with the cluster. Examining the Infrared Array Camera colors of these sources, we find that one object is likely to be an AGN. Assuming that the other 24 μm sources are powered by star formation, their IR luminosities imply star formation rates $\sim 100\, M_\odot$ yr^{-1}. We find that three of these sources are located at projected distances of <250 kpc from the cluster center, suggesting that a large amount of star formation may be taking place in the cluster core, in contrast to clusters at low redshift.

Key words: galaxies: active – galaxies: clusters: individual (XMMXCS J2215.9−1738) – galaxies: star formation – X-rays: galaxies: clusters

Online-only material: color figures

1. INTRODUCTION

The universe at high redshift is a much more active place than we see locally. Radio and far-infrared (far-IR) studies have shown that the comoving star formation rate (SFR) density increases by a factor of ≈10 from $z = 0$ to $z \approx 1$ (e.g., Seymour et al. 2008; Magnelli et al. 2009), and continues rising toward higher redshifts, peaking at $z \approx 3$ (Bouwens et al. 2009). The fraction of galaxies with active galactic nuclei (AGNs) is also seen to be much higher when the universe was young: current observations suggest that the space density of the brightest AGNs peaks at $z \approx 2$–3 (Assef et al. 2010; Silverman et al. 2005). Observations in the local universe show that the stellar mass of galactic bulges is correlated with the mass of nuclear supermassive black holes (e.g., Ferrarese & Merritt 2000; Gebhardt et al. 2000), suggesting that AGNs play a major role in the growth of stellar mass. Simulations suggest that interactions and mergers between gas-rich galaxies drive this process, both by providing fuel for AGNs and triggering starburst activity in galactic nuclei (e.g., Granato et al. 2004; Hopkins et al. 2008). Eventually, gas heating by the AGN (feedback) reaches such a level that star formation is shut down, leaving the stellar population of the host galaxy to evolve passively. The quenching of star formation in massive galaxies by AGN feedback is a crucial ingredient in the latest semianalytic models of galaxy formation, bringing the models into much closer agreement with observations (e.g., De Lucia et al. 2006; Croton et al. 2006; Bower et al. 2006; Somerville et al. 2008).

A connection between local environment, star formation, and AGN is therefore expected in this theoretical picture. Intriguingly, recent studies of the dependence of SFR on local galaxy density using large samples of field galaxies indicate that SFR increases with increasing local density at $z \approx 1$ (Elbaz et al. 2007; Cooper et al. 2008), whereas the opposite is observed in the local universe (e.g., Lewis et al. 2002; Balogh et al. 2004). This situation is mirrored to some extent in galaxy clusters. Although these systems are dominated by quiescent, early-type

galaxies—primarily "red-and-dead" ellipticals—and continue to host substantial populations of these objects up to the highest redshifts observed (e.g., Blakeslee et al. 2003; Lidman et al. 2008; Mei et al. 2009; Hilton et al. 2009), an increasing fraction of star-forming, late-type galaxies are seen in clusters at higher redshifts (e.g., Butcher & Oemler 1984; van Dokkum et al. 2000; Ellingson et al. 2001; Smith et al. 2005). However, recent mid-IR observations of clusters conducted using the *Spitzer Space Telescope* show that a significant amount of this increased star formation at high redshift is obscured by dust (Geach et al. 2006; Marcillac et al. 2007; Saintonge et al. 2008; Haines et al. 2009b), and therefore the amount of star formation in clusters has previously been underestimated.

The AGN fraction in clusters is also seen to rise with redshift. Martini et al. (2009) report an eightfold increase in the number of AGNs in clusters at $z = 1$ compared to in the local universe. Similarly, Galametz et al. (2009) find that IR-selected clusters in the Infrared Array Camera (IRAC) Shallow Cluster Survey (Eisenhardt et al. 2008) show a clear excess of AGNs at high redshift, with the AGN fraction increasing by a factor of 3 from $0.5 < z < 1.0$ to $1.0 < z < 1.5$. However, it is not yet clear if the AGN fraction is higher in clusters than in the field, nor if the AGN fraction is evolving more rapidly in dense environments.

In this paper, we use *Chandra* X-ray observations and mid-IR observations taken using the *Spitzer Space Telescope* to characterize the AGN and dusty star-forming population of the $z = 1.46$ cluster XMMXCS J2215.9−1738 (hereafter J2215), which was discovered in the ongoing optical follow up of the *XMM* Cluster Survey (XCS; Romer et al. 2001; Sahlén et al. 2009). J2215 is the second highest redshift X-ray-selected cluster known, following the recent discovery of a $z = 1.62$ cluster in the Subaru/XMM-Newton Deep Field (Tanaka et al. 2010, Papovich et al. 2010). The discovery of J2215 and an analysis of its X-ray properties using *XMM-Newton* data were reported in Stanford et al. (2006, hereafter S06). We presented a first study of the dynamical state of the cluster and measurement of its velocity dispersion using additional Very Large Telescope and Keck spectroscopy in Hilton et al. (2007, hereafter H07). Most recently, we have used *Hubble Space Telescope* (*HST*) imaging and ground-based near-IR data obtained at the Subaru telescope to perform a detailed examination of the morphologies of the cluster galaxies and the red sequence within <0.75 Mpc of the cluster core (Hilton et al. 2009, hereafter H09).

The structure of this paper is as follows. In Section 2, we report revised measurements of the cluster X-ray properties obtained through a joint spectroscopic analysis of the *Chandra* and *XMM-Newton* data, taking into account the effect of X-ray point sources that were unresolved in the *XMM-Newton* data used in S06. In Section 3, we briefly review the optical and ground-based near-IR data used in this paper, before describing new photometry obtained using IRAC (Fazio et al. 2004) that extends wavelength coverage of the cluster into the rest-frame near-IR. We describe additional spectroscopic observations obtained at the Keck and Gemini observatories during 2008–2009 in Section 4, where we also present an updated measurement of the cluster velocity dispersion. Mid-IR (24 μm) observations of the cluster obtained using the Multiband Imaging Photometer for *Spitzer* (MIPS) are described in Section 5. We characterize the properties of cluster 24 μm and X-ray sources in terms of star formation or AGN activity in Section 6. Finally, we discuss our findings in comparison with lower redshift studies of clusters in Section 7.

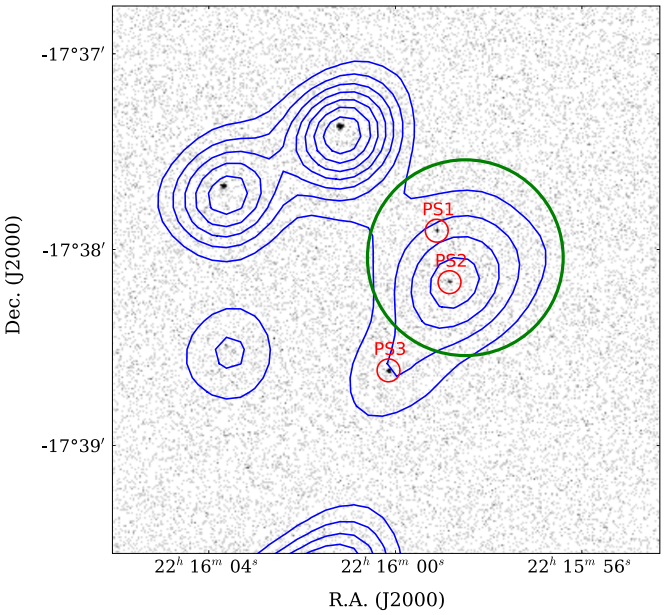

Figure 1. *Chandra* ACIS-S image of J2215.9−1738 with the *XMM-Newton* EPIC contours (Stanford et al. 2006) overlaid. The large circle marks the 30″ radius extraction region used for the *XMM-Newton* spectroscopic analysis in both Stanford et al. (2006) and this work. The two unlabeled point sources to the northeast were previously known from the *XMM-Newton* observations and taken into account in the analysis presented in Stanford et al. (2006). The three previously unknown point sources which contaminated the original *XMM* detection are labeled PS1–3.

(A color version of this figure is available in the online journal.)

We assume a concordance cosmology of $\Omega_m = 0.3$, $\Omega_\Lambda = 0.7$, and $H_0 = 70$ km s^{-1} Mpc^{-1} throughout, where Ω_Λ is the energy density associated with a cosmological constant. All magnitudes are on the AB system (Oke 1974), unless otherwise stated.

2. X-RAY OBSERVATIONS

2.1. Joint XMM–Chandra Spectroscopic Analysis

J2215 is detected as an extended X-ray source in the XCS, but the low resolution of *XMM-Newton*, especially off-axis, could lead to significant contamination of the cluster emission by unresolved point sources. The comoving space density of bright AGN rises steeply beyond $z > 0.5$ and at $z \approx 1.5$ is nearing its peak (Silverman et al. 2005). There is therefore a much higher probability of a high-redshift cluster such as J2215 containing an X-ray bright AGN compared to clusters in the local universe.

To check for point-source contamination, we obtained a 56.2 ks *Chandra* ACIS-S observation of the cluster,[12] resulting in 55.3 ks after cleaning to remove periods of high background. The ACIS-S image reveals two point sources within the 30″ radius extraction region used for the *XMM-Newton* spectroscopic analysis described in S06. Another previously unidentified point source is detected ≈12″ outside the extraction region used in the S06 analysis, but some flux from this object is spread into the extraction region by the larger point-spread function (PSF) of *XMM-Newton*.

Figure 1 shows the ACIS-S image with the *XMM-Newton* contours overlaid (newly identified point sources in the *Chandra* data are marked PS1–3). The three sources are detected with only 23, 27, and 48 counts, respectively, but despite this it

[12] *Chandra* ObsID 7919 and 8566.

Table 1
Properties of X-ray Point Sources from *Chandra* ACIS-S Spectroscopy

ID	R.A.	Decl.	z	N_H[a]	α	f_X[b]	EF[c]	CF[d]	$L_{X(0.5-2.0\ keV)}$[e]	$L_{X(2-10\ keV)}$[e]
PS1	22 15 59.115	−17 37 54.24	1.462	$1.6^{+2.6}_{-0.8}$	$2.3^{+1.1}_{-0.8}$	1.0	0.75	0.065	0.36	0.25
PS2	22 15 58.857	−17 38 09.98	1.453	$0.67^{+0.91}_{-0.47}$	$4.1^{+1.2}_{-0.8}$	1.3	0.63	0.071	1.2	0.14
PS3	22 16 00.148	−17 38 37.04	2.5[f]	44^{+27}_{-14}	$1.9^{+0.8}_{-0.7}$	1.3	0.09	0.009	5.4	6.7

Notes. Units of right ascension are hours, minutes, and seconds, and units of declination are degrees, minutes, and seconds (J2000).
[a] Hydrogen column density ($\times 10^{22}$ cm^{-2}).
[b] Flux ($\times 10^{-15}$ erg s^{-1} cm^{-2}) in the 0.5–2.0 keV band. The uncertainty in these values is ≈30%–50%.
[c] The fraction of the source flux that is estimated to be within the extraction region used for the *XMM-Newton* spectroscopic analysis.
[d] Estimate of the fraction that the source contributes to the cluster flux measured by Stanford et al. (2006).
[e] Unabsorbed luminosity ($\times 10^{44}$ erg s^{-1}) in the indicated energy band.
[f] The redshift for PS3 is a low-confidence photometric estimate.

is possible to fit their spectra with simple power-law models including photoelectric absorption (WABS, using the XSPEC package; Arnaud 1996) in order to constrain their properties. The results of the spectral fitting are shown in Table 1.

The spectral properties are consistent with the sources being AGN, with power-law indices in the typical range for these objects. The fluxes of the sources span the range (1.0–1.3) × 10^{-15} erg s^{-1} cm^{-2} in the 0.5–2.0 keV band. Sources PS1 and PS2 are spectroscopically confirmed cluster members which show 3727 Å [O II] emission but not broad lines (see Section 4). Source PS3 is also a 24 μm source (see Section 5), but is not spectroscopically confirmed despite 8 hr of integration on this object being obtained at Gemini (see Section 4). The object does have a low-confidence photometric redshift from the analysis of H09 placing the object in the background of the cluster at $z_p \approx 2.5$. Assuming these redshifts, we estimate luminosities for the X-ray point sources after removing the effects of intrinsic absorption within the host galaxies. We find that the sources have unabsorbed luminosities spanning the range $L_{X(2-10\ keV)} \approx (0.1–6) \times 10^{44}$ erg s^{-1}, typical of AGN rather than starburst galaxies. We list the source properties in Table 1 and discuss the properties of the AGN further in Section 6.1.

In order to calculate the fraction of flux from these point sources contaminating the cluster emission, we used the SCISIM[13] package to produce simulated images of the sources detected by *Chandra* blurred by the *XMM-Newton* PSF. The estimated fraction of the flux from each point source that falls within the *XMM-Newton* extraction region is also listed in Table 1. We find that the point sources contribute ≈15% of the total flux measured within the extraction region.

To take into account the effect of the point-source contamination on the cluster properties measured using *XMM-Newton* (S06), it was necessary to undertake a joint fit of the *XMM-Newton* and *Chandra* data. A model consisting of three absorbed power-law plus an absorbed MEKAL (Mewe–Kaastra–Liedahl) plasma model was jointly fitted to the *XMM-Newton* spectra from the extraction region and *Chandra* spectra of the individual point sources with the flux fractions in the extraction region calculated from SCISIM taken into account. The resulting temperature from this analysis is $T = 4.1^{+0.6}_{-0.9}$ keV.

A temperature $T = 7.4^{+2.7}_{-1.8}$ keV (90% confidence) was measured in the analysis of S06 based on the *XMM-Newton* data alone. S06 also considered the possibility of contamination from an unresolved central point source, estimating a lower temperature of $T = 6.5^{+2.6}_{-1.8}$ keV (90% confidence) in that case. Both of these temperature estimates are somewhat higher

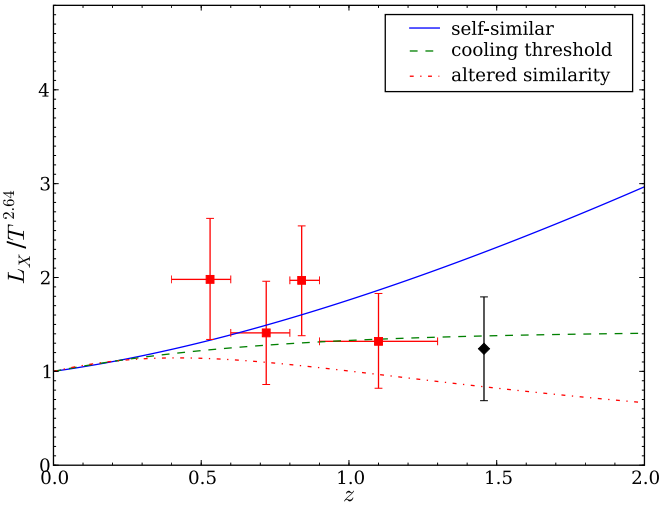

Figure 2. Comparison of $L_X/T^{2.64}$ (i.e., assuming the slope of the Markevitch 1998 L_X–T relation) for J2215.9−1738 (diamond point; the error bar is estimated using a bootstrap resampling technique) with the predicted evolution of the normalization of the L_X–T relation for the cases of self-similarity ($E(z)$), cooling threshold ($t_0/[E(z)t(z)]$), and altered similarity ($t_0^2/[E(z)^3 t(z)^2]$; see Voit 2005 for a description of these latter two models). The square points are the data of Maughan et al. (2006); vertical error bars are equal to the weighted standard deviation at each redshift, horizontal error bars indicate the width of each redshift bin.

(A color version of this figure is available in the online journal.)

than the temperature measured from the joint *Chandra–XMM* analysis presented here.

The bolometric luminosity of the cluster is found to be $L_X = (2.92^{+0.24}_{-0.35}) \times 10^{44}$ erg s^{-1}, extrapolated to a radius of 2 Mpc assuming a β model with $\beta = 0.63$ and core radius $r_c = 52$ kpc. This is ≈33% lower than the equivalent measurement reported in S06. As discussed in H07, a comparison of the S06 luminosity and temperature measurements indicates that the cluster is underluminous compared to the value expected if the L_X–T relation evolves self-similarly with redshift. The cluster was found to follow the evolution expected in the Voit (2005) analytic models that include the effects of non-gravitational heating and radiative cooling (see also Voit & Ponman 2003 and the discussion in Hilton et al. 2007). We find that this remains the case using the luminosity and temperature estimates obtained in the joint *Chandra–XMM* analysis presented here, although the size of the deviation from the self-similar $E(z)$ scaling is reduced to the ≈2σ level. This is illustrated in Figure 2, which shows the predicted evolution of the normalization of the L_X–T relation for the self-similar case, in comparison

[13] http://xmm.vilspa.esa.es/scisim/release/

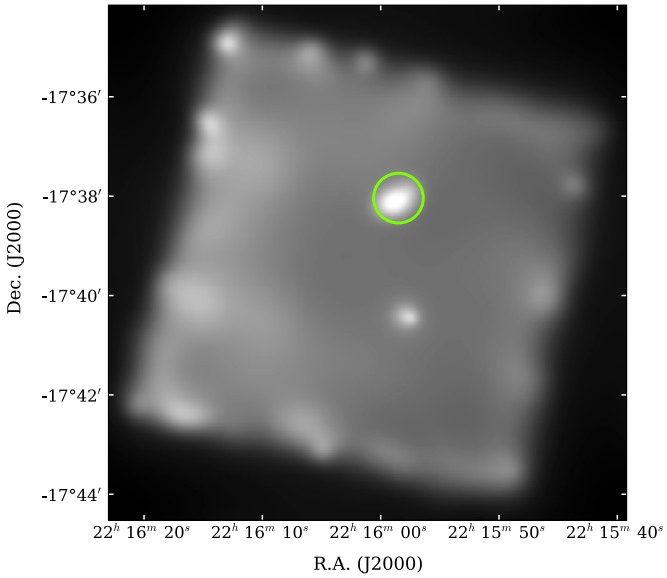

Figure 3. Adaptively smoothed (after point-source subtraction) *Chandra* ACIS-S image of the field of J2215.9−1738. The 30″ radius extraction region used for the *XMM-Newton* spectroscopic analysis is shown by the circle. The cluster extended emission is clearly visible, and is detected at the ≈9σ level. Another faint extended source, BLOX J2215.9−1740.4 (Dietrich et al. 2007, which is also detected in the XCS extended source catalog), is clearly visible below J2215.9−1738. No other significant sources are seen.

(A color version of this figure is available in the online journal.)

to the "cooling threshold" ($t_0/[E(z)t(z)]$) and "altered similarity" ($t_0^2/\left[E(z)^3 t(z)^2\right]$) models of Voit (2005). We assume the slope of the L_X–T relation measured by Markevitch (1998) in comparing the data to the models. The uncertainty on the value of $L_X/T^{2.64}$ inferred from the J2215 luminosity and temperature measurements is estimated using a bootstrap resampling technique.

2.2. Extended Emission

In addition to studying the point sources in the region of J2215, for which the *Chandra* telescope is most suited due to its high spatial resolution, we also attempted to identify extended emission from the cluster in the *Chandra* imaging data alone. Given the considerably lower effective area of *Chandra* and significantly lower exposure time for these observations compared to the *XMM-Newton* observations, the amount of information that can be obtained from such a detection is limited, but does provide an independent confirmation of the cluster X-ray emission. In order to study extended emission in the *Chandra* data we first removed flux due to the detected point sources (an easy task given the small, well-characterized PSF of *Chandra*), and produced a 0.3–2.0 keV band image (the energy band was chosen to maximize the signal-to-noise ratio, S/N). The CIAO task `csmooth` was then used to adaptively smooth the image.

The resulting smoothed image can be seen in Figure 3, where we have highlighted the 30″ radius spectral extraction region used for the *XMM-Newton* spectroscopic analysis. It can be seen that there is a strong extended source coincident with the position of J2215. The extended emission is detected at the ≈9σ level, with 123 counts in the 0.3–2.0 keV band. Unfortunately, due to the low number of counts, we are unable to place comparable constraints on the cluster temperature to those obtained with the *XMM-Newton* data from the *Chandra* data alone, although the spectrum is consistent with the temperature being in the 3–6 keV range.

3. OPTICAL AND NEAR-INFRARED IMAGING

We have previously obtained imaging of J2215 at both optical and near-IR wavelengths using a variety of different telescopes and instruments. Wide field coverage is provided by *I*-band data taken from the ESO Imaging Survey (Dietrich et al. 2006), and by K_s-band imaging from the Palomar 5 m telescope; these data are described in S06, and the overlapping area between them covers an 8′ × 8′ area centered on the cluster. The K_s-band data in this case reach a 5σ limiting magnitude of ≈21.8 (AB). Much deeper observations of the central 3′ × 3′ of the cluster field have been obtained using *HST* (i_{775}, z_{850}) and Subaru (J, K_s). These data reach ≈2.5 mag deeper at K_s than the Palomar data, and were used to construct a photometric redshift catalog (H09). The *HST* data were obtained as part of a supernova search in high-redshift clusters (Dawson et al. 2009). In the present study we add imaging with the *Spitzer* IRAC instrument to this data set, which extends the wavelength coverage into the rest-frame near-IR at the cluster redshift.

3.1. Spitzer IRAC Data

IRAC imaging of J2215 was obtained through Program 50333 using all four channels (3.6, 4.5, 5.8, and 8.0 μm) on 2008 July 12. The frame time was 100 s and 15 exposures were obtained in a medium scale cycling dither pattern. The basic calibrated data (BCD) images were corrected for muxbleed and pulldown and then mosaiced using `MOPEX` (Makovoz & Khan 2005).

Photometry was performed using `SExtractor` (Bertin & Arnouts 1996) in a two-stage process. In the first stage, an initial set of catalogs were generated for each IRAC band, which were then merged by associating objects located within <1.″2 of each other across the catalogs (note the astrometry of the IRAC mosaics is accurate to <0.″2). The positions of objects in these catalogs were used to register the IRAC mosaics to a common pixel coordinate system. These registered mosaics were then trimmed to a region of 5.′9 × 6.′6 with coverage in all IRAC bands, centered on the cluster X-ray position. In the second stage, we ran `SExtractor` in dual-image mode, extracting a 3.6 μm selected catalog from the registered and trimmed IRAC images in each band using a consistent set of photometric apertures.

We measured fluxes through 4″ diameter circular apertures, adopting aperture corrections to total magnitudes of −0.350 ± 0.040, −0.350 ± 0.040, −0.540 ± 0.040, and −0.660 ± 0.020 mag for IRAC channels 1–4, respectively, as measured by Barmby et al. (2008; note that aperture corrections consistent with these values were also found by Papovich et al. 2006 and Pérez-González et al. 2008b). We use these aperture-corrected magnitudes to measure colors between the IRAC bands (see Section 6.1).

The uncertainties in the aperture corrections were added in quadrature to the photometric uncertainties reported by `SExtractor`; however, at this stage the photometric errors are underestimated due to the effect of resampling the IRAC images during the production of the mosaics, which introduces correlations in the noise between adjacent pixels. This additional source of uncertainty is not taken into account in the `SExtractor` photometric errors. We correct for this effect using simulations, in a similar manner to that described by Barmby

et al. (2008). We measure the background flux through 100 non-overlapping 4″ diameter apertures placed at random locations in each IRAC mosaic that do not coincide with detected objects, repeating this process 1000 times. We scale the aperture-corrected SExtractor photometric errors by the median rms background flux measured from these simulations divided by the median SExtractor flux error of the detected objects. The scale factors applied to the uncertainties in the total aperture magnitudes were 2.2, 1.8, 2.5, and 1.9 across IRAC channels 1–4, respectively.

The IRAC catalog was cross-matched against the K_s-selected catalogs described above using a 1.″2 matching radius. Clearly, given the much larger PSF of IRAC (1.″67–1.″98) compared to these other catalogs, many sources are blended in the cluster center; in each case we choose the nearest match, and will note such affected objects where necessary in the subsequent analysis.

4. OPTICAL SPECTROSCOPY

4.1. Observations and Data Reduction

Redshifts for 17 galaxies concordant with the cluster redshift were reported in H07. We have observed J2215 using further six slit masks since that work: five with the DEep Imaging and Multi-Object Spectrograph (DEIMOS; Faber et al. 2003) on the 10 m Keck II telescope, plus one additional mask observed with the Gemini Multi-Object Spectrograph (GMOS; Hook et al. 2003) on the 8 m Gemini South telescope. Redshifts for galaxies within 3′ of the cluster center from three of the additional DEIMOS masks (obtained in 2007 September and 2008 September) were included in the catalog included in H09. The two DEIMOS masks and the GMOS mask observed in 2009 were designed to prioritize objects detected in our mid-IR imaging (see Section 5). We now describe the observations and data reduction for each instrument in turn.

4.1.1. DEIMOS

For all masks, DEIMOS was used with the 600ZD grating, which is blazed at 7500 Å and has dispersion 0.65 Å pixel^{-1}, in conjunction with the OG515 order sorting filter. This setup provides typical wavelength coverage from 5000 to 10000 Å. Slits of width 1.″2 and minimum length 5″ were used in all slit masks. Each mask contained typically ≈110 slitlets, spread across the 16.′7 × 5.′0 field of view of DEIMOS.

A total of five masks were observed with DEIMOS subsequent to the analysis presented in H07. We observed one mask on UT 2007 September 10, obtaining 3 × 1800 s of exposures in clear conditions with 0.″7 seeing. Two masks were observed on UT 2008 September 1 and 2 in mostly clear conditions. The seeing was typically 0.″6 on September 1, rising to 0.″9 on the following night. In these masks, we preferentially targeted galaxies close to the red sequence with photometric redshifts concordant with the cluster redshift from the catalog presented in H09. We obtained 5 × 1800 s of integration time through the mask observed on September 1 and 7 × 1800 s through the second mask, which was observed on the following night. Finally, on UT 2009 October 18 and 19 we observed two more masks, in which 24 μm sources (see Section 5) were prioritized. These observations were carried out in clear conditions with 0.″7–0.″8 seeing. We obtained 5 × 1800 s of exposures for each of these masks, observing one mask on each night.

The DEIMOS data were reduced as described in H07, using version 1.1.4 of spec2d, the pipeline developed for the DEEP2 galaxy redshift survey (Davis et al. 2003).

4.1.2. GMOS

Service mode observations of J2215 were obtained using GMOS over the period UT 2009 August 23–September 23. GMOS was used in nod-and-shuffle mode (Glazebrook & Bland-Hawthorn 2001), which allows both improved sky subtraction and shorter slit lengths compared to more conventional techniques. We used the R400 grating, which for our observations has dispersion 1.34 Å pixel^{-1} due to 2 × 2 binning of the detectors. The OG515 order blocking filter was used, giving a nominal wavelength coverage of 5400–9700 Å when used in combination with our chosen grating. One mask was observed, containing 34 target slitlets of length 3″ and width 1″. A total of 15 × 1920 s of exposures were obtained, divided equally among three different central wavelengths (7500, 7550, and 7600 Å), in order to obtain coverage over the gaps between the GMOS CCDs. We also varied the detector translation assembly offset by ±2 pixels in the y-direction to mitigate against defects in the CCDs that cause artifacts in very deep nod-and-shuffle observations. The nod-and-shuffle cycle time of our observations was 120 s, and our offset size was chosen such that the object was visible in the slit at both nod positions, to maximize the on-source integration time. Each of our 1920 s exposures therefore consisted of 16 nod-and-shuffle cycles. The relevant observing constraints chosen for the queue mode observations were: 85 percentile image quality (i.e., seeing <1.″2 in the I band); and 50 percentile sky transparency (i.e., photometric conditions).

The data were reduced using routines from v1.8 of the Gemini IRAF[14] package. The data for each night and grating angle combination were processed separately. Briefly, the data were bias subtracted in the standard manner, sky subtracted (using the gnsskysub task), and then flat fielded. Data from individual chips were then mosaiced together, before being cut into separate FITS extensions corresponding to each slitlet using a custom written tool. Wavelength calibration was performed using a cross-correlation technique, which was found to be accurate to 0.3 Å. All data were then combined using a median average, rejecting bad pixels using a mask constructed from nod-and-shuffle dark frames. Finally, the pairs of spectra corresponding to each nod position were combined appropriately and one-dimensional spectra were extracted using a simple boxcar algorithm.

4.2. Redshift Measurements

Redshifts were measured using a technique similar to that described in H07. Briefly, the spectra were cross-correlated against a subset of the Sloan Digital Sky Survey (SDSS) spectral templates,[15] plus the Luminous Red Galaxy template of Eisenstein et al. (2003), using the xcsao task in the rvsao IRAF package (Kurtz & Mink 1998). All spectra were visually inspected to check the accuracy of the redshift solution; where the cross-correlation redshift solution was clearly incorrect, the redshift was measured from visually identified spectral features. Due to the limited wavelength coverage of the SDSS templates at blue wavelengths in the rest frame at the cluster redshift, and the additional complication of residual sky emission at wavelengths

[14] IRAF is distributed by the National Optical Astronomy Observatory, which is operated by the Association of Universities for Research in Astronomy, Inc., under cooperative agreement with the National Science Foundation.

[15] http://www.sdss.org/dr5/algorithms/spectemplates/index.html

approaching ∼10000 Å, most (≈2/3) of the redshifts for cluster members were measured by the visual inspection method rather than using the cross-correlation method. However, the cross-correlation technique is very efficient for measuring the redshifts of lower redshift galaxies, of which a significant number are contained in our masks, each of which typically targeted ∼100 galaxies out to ∼11′ away from the cluster center.

Redshifts were assigned a quality flag according to the following scheme: $Q = 3$ (completely unambiguous, at least two positively identified spectral features); $Q = 2$ (high confidence that the redshift is correct, one clearly detected feature); $Q = 1$ (significant doubt that the redshift is correctly identified, one or more weakly detected features). As discussed below, a significant fraction of the cluster members are identified as 3727 Å [O II] emitters, including 15 objects with $Q = 2$ rather than $Q = 3$ redshifts. Although the redshifts of these objects are in most cases determined from a single emission line, we are reasonably confident that the line identification is correct, as no emission lines are seen blueward down to ∼6000 Å.

A total of 16 objects now have multiple reasonably secure redshift measurements ($Q \geqslant 2$) across different slit masks. We adopt the rms scatter of the residuals between these multiple redshift measurements as our estimate of the total (i.e., random+systematic) redshift error, finding $\Delta z = 1.4 \times 10^{-3}$. We list the redshifts of all galaxies found within ±3000 km s^{-1} of the recession velocity corresponding to the cluster redshift of $z = 1.46$ in Table 2. A total of 44 galaxies now have $Q \geqslant 2$ redshifts in the range $1.435 < z < 1.485$, an increase of 26 galaxies over the catalog presented in H07.

Approximately two-third of the galaxies for which $Q \geqslant 2$ spectroscopic redshifts have been obtained show 3727 Å [O II] emission (see Table 2). This includes 13 galaxies located within a projected distance of <250 kpc from the cluster center, and implies that a significant amount of star formation could be taking place even in the inner regions of the cluster, which is not found to be the case in lower redshift clusters. However, several studies have shown that [O II] emission is often not due to star formation at high redshift, and is instead associated with Seyfert-type AGNs or low-ionization nuclear emission-line regions (LINERs; Heckman 1980), which can also be found in otherwise passively evolving galaxies (Yan et al. 2006; Lemaux et al. 2010). A significant fraction of [O II] emitting galaxies in the cluster core has also been found by Hayashi et al. (2010), using narrow-band imaging that reaches to an [O II] flux limit $\geqslant 1.4 \times 10^{-17}$ erg s^{-1} (corresponding to equivalent width ⩾35 Å), allowing galaxies with SFR > 2.6 $M_\odot$ yr^{-1} to be detected. Hayashi et al. (2010) report that ≈30% of the cluster members within a projected distance of 250 kpc from the cluster center are [O II] emitters. Given the heterogeneous nature of our spectroscopic target selection, and the potential for selection biases (for example, the relative ease of identifying [O II] emission at the cluster redshift compared to securing redshifts for passively evolving member galaxies), it is unfortunately not possible to infer the fraction of star-forming galaxies within the cluster based on our spectroscopic data alone.

4.3. Cluster Line-of-sight Velocity Distribution

We plot in Figure 4 the velocity distribution of all 44 galaxies with $Q \geqslant 2$ redshifts listed in Table 2. Calculating the velocity dispersion for the whole sample of 44 galaxies using a biweight scale estimator (Beers et al. 1990), and applying the Danese et al. (1980) correction for broadening of the distribution due to redshift measurement errors (see Section 4.2), we measure the line-of-sight velocity dispersion to be $\sigma_v = 890 \pm 110$ km s^{-1}. However, this includes galaxies located up to ≈4.6 Mpc away from the cluster center, and not all galaxies at large radial distances may be gravitationally bound to the cluster. Using the iterative method of calculating σ_v and R_{200} from the redshift data as described in H07, we obtain a lower value of $\sigma_v = 720 \pm 110$ km s^{-1} using only the 31 galaxies within R_{200}, which we estimate to be $R_{200} = 0.8 \pm 0.1$ Mpc. We estimate the cluster redshift to be $z = 1.457 \pm 0.001$ by applying the biweight location estimator to this galaxy sample, in agreement with the result of H07. We highlight the velocity distribution corresponding to this membership selection in Figure 4.

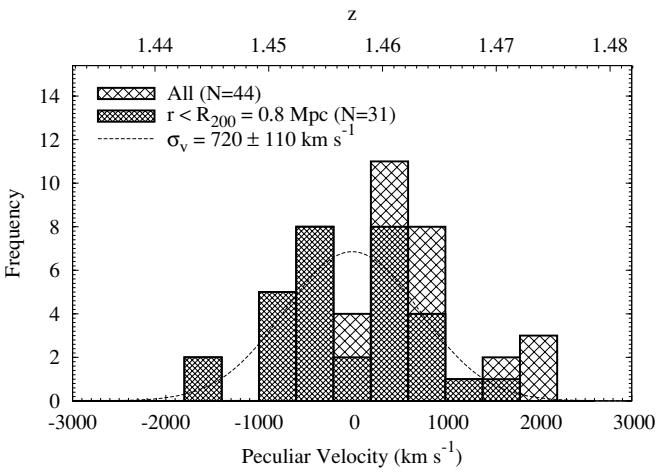

Figure 4. Peculiar velocity distribution of J2215.9−1738. Only galaxies with reasonably secure ($Q \geqslant 2$) redshifts are included. The shading distinguishes between the sample of 31 galaxies located at radial distance $r < R_{200}$ (see Section 4.3), and the complete sample of 44 galaxies with $1.435 < z < 1.485$. The dashed line shows a Gaussian with σ equal to the velocity dispersion estimated using galaxies within R_{200}.

The value of σ_v quoted here is higher than the value of 580 ± 140 km s^{-1} estimated using the smaller redshift catalog presented in H07, but agrees with the previous measurement at better than $\lesssim 0.8\sigma$. In H07, we noted a discrepancy between the temperature implied by the galaxy velocity dispersion and the X-ray temperature measured in S06, suggesting that the cluster gas has 2–3 times the kinetic energy of the cluster galaxies. The joint *XMM–Chandra* spectroscopic X-ray analysis presented in Section 2 now reconciles the velocity and X-ray measurements: for $\sigma_v = 720$ km s^{-1}, the predicted X-ray temperature is $T_{\sigma_v} = 3.2 \pm 0.9$ keV, compared to the revised X-ray measurement of $T = 4.1^{+0.6}_{-0.9}$ keV, and therefore agrees at $\lesssim 0.7\sigma$. The cluster lies on the σ_v–T relation expected if there is equipartition of gravitational potential energy between the gas and the galaxies following this revised analysis.

In H07, we also presented mild evidence that the cluster velocity distribution is bimodal, and it is clear from inspection of Figure 4 that the additional redshift data have not erased this signal. We performed the Hartigan & Hartigan (1985) test of unimodality using the sample of 31 galaxies within R_{200} as estimated above, measuring the value of the dip statistic to be 0.0668. Simulations show that the probability to exceed this dip value when drawing from a Gaussian distribution with σ equal to the measured line-of-sight velocity dispersion is $P = 0.103$. Therefore, the expanded spectroscopic catalog does not strongly favor a bimodal velocity distribution using this sample. We also used the KMM algorithm (Kaye's Mixture Model; Ashman et al. 1994) to test for bimodality. This algorithm tests whether a mixture of n Gaussian distributions is a better description of a

Table 2
Galaxies within ±3000 km s^{-1} (Rest Frame) of the Recession Velocity Corresponding to the Redshift of J2215.9−1738 ($z = 1.46$)

ID	R.A. (J2000)	Decl. (J2000)	z_a	Q^b	Method[c]	I^d	$K_s{}^e$	H09[f]	r (arcmin)	r (Mpc)	[O II][g]
1	22 15 58.464	−17 37 58.58	1.452	3	V	23.63	20.90	742	0.066	0.033	···
3	22 15 58.872	−17 37 59.26	1.451	3	V	23.30	21.05	748	0.104	0.053	···
4	22 15 58.056	−17 38 04.59	1.465	2	V	···	23.60	789	0.111	0.057	···
5	22 15 59.040	−17 38 02.54	1.454	2	V	22.72	20.86	770	0.129	0.065	✓
6	22 15 58.488	−17 38 10.53	1.465	3	X	23.73	20.57	824	0.134	0.068	···
7	22 15 59.080	−17 38 02.40	1.459	2	V	22.72	20.86	770	0.138	0.070	✓
10	22 15 58.848	−17 38 09.85	1.453	2	V	22.75	21.77	821	0.148	0.075	✓
16	22 15 59.136	−17 37 54.22	1.462	3	X	24.36	20.72	712	0.205	0.104	✓
18	22 15 59.376	−17 38 09.88	1.467	3	V	24.56	23.89	823	0.242	0.123	✓
19	22 15 57.432	−17 37 57.90	1.454	2	V	···	23.05	754	0.266	0.135	✓
30	22 15 57.192	−17 38 07.80	1.450	3	X	23.24	22.05	810	0.324	0.164	✓
35	22 15 57.240	−17 37 53.22	1.454	3	V	23.69	21.41	708	0.338	0.171	✓
36	22 15 57.720	−17 37 45.55	1.451	2	V	24.17	20.91	653	0.338	0.172	✓
38	22 15 58.752	−17 37 40.76	1.460	2	X	···	22.33	631	0.367	0.186	✓
39	22 15 56.928	−17 38 04.70	1.445	3	V	23.03	21.82	786	0.376	0.191	✓
44	22 15 58.344	−17 37 37.30	1.453	3	V	24.11	22.71	629	0.422	0.214	✓
53	22 16 00.384	−17 37 50.59	1.451	3	X	23.52	20.99	692	0.491	0.249	✓
57	22 16 00.648	−17 37 51.67	1.471	2	V	23.66	21.17	696	0.543	0.275	···
59	22 15 56.184	−17 37 49.90	1.454	3	X	23.64	20.57	688	0.590	0.300	···
62	22 15 56.016	−17 37 55.05	1.460	2	V	24.41	23.88	723	0.605	0.307	···
63	22 16 00.096	−17 37 33.92	1.454	3	V	···	22.86	591	0.609	0.309	✓
65	22 15 56.058	−17 37 49.90	1.461	2	V	···	···	···	0.618	0.314	✓
66	22 15 59.472	−17 38 37.39	1.457	3	X	23.09	22.77	1018	0.626	0.318	✓
77	22 16 00.096	−17 38 42.61	1.463	2	V	23.57	22.25	1047	0.769	0.390	···
82	22 15 56.544	−17 37 21.36	1.446	2	V	23.67	21.49	526	0.829	0.421	✓
105	22 16 00.360	−17 38 57.69	1.456	2	V	···	21.64	1130	1.021	0.518	✓
106	22 15 55.200	−17 37 22.36	1.460	2	V	23.65	21.36	538	1.032	0.524	···
120	22 16 03.432	−17 37 51.24	1.462	2	V	24.11	22.82	697	1.190	0.604	✓
161	22 15 54.000	−17 39 01.65	1.464	2	V	23.19	21.29	1149	1.457	0.739	✓
162	22 15 52.464	−17 37 46.05	1.461	2	V	22.77	20.99	···	1.464	0.743	✓
176	22 15 56.160	−17 36 37.80	1.455	3	V	24.98	23.03	96	1.518	0.770	✓
203	22 16 05.400	−17 38 17.48	1.465	3	X	···	22.75	859	1.663	0.844	✓
232	22 15 51.648	−17 37 11.74	1.461	3	X	24.07	20.77	···	1.839	0.933	···
264	22 16 02.448	−17 39 53.46	1.456	2	V	···	21.12	···	2.075	1.053	✓
292	22 15 57.960	−17 40 20.35	1.465	3	V	22.17	19.36	···	2.301	1.168	···
301	22 16 02.424	−17 40 09.08	1.475	2	X	22.67	···	···	2.308	1.171	···
303	22 15 54.864	−17 40 12.97	1.475	2	X	23.71	···	···	2.341	1.188	···
358	22 16 09.504	−17 38 26.16	1.461	3	X	23.81	···	···	2.651	1.345	···
371	22 16 09.888	−17 38 26.41	1.459	2	V	···	20.67	···	2.742	1.392	✓
400	22 15 58.944	−17 41 01.28	1.470	2	V	23.41	21.33	···	2.982	1.513	✓
439	22 16 10.296	−17 36 22.96	1.463	3	X	23.54	···	···	3.264	1.656	✓
494	22 16 10.728	−17 40 24.31	1.463	3	V	23.43	22.42	···	3.751	1.904	···
505	22 16 04.104	−17 34 23.37	1.474	3	X	23.41	···	···	3.889	1.973	✓
883	22 15 50.832	−17 29 09.45	1.458	3	X	22.54	···	···	9.070	4.603	✓

Notes. Units of right ascension are hours, minutes, and seconds, and units of declination are degrees, minutes, and seconds.
[a] The redshift uncertainty is measured to be 1.4×10^{-3}; see Section 4.2.
[b] An additional 14 objects with $Q = 1$ (insecure) redshifts are not listed in this table.
[c] Redshift measurement method: V = from visually identified features; X = from cross-correlation with spectral templates (see Section 4.2).
[d] Measured in ESO Imaging Survey data (Dietrich et al. 2006); magnitudes have been converted to the AB system using $I(\mathrm{AB}) = I(\mathrm{Vega}) + 0.41$. If no value is given, the object was not detected. ID 65 is detected in *HST* i_{775} imaging of the cluster (described in Hilton et al. 2009).
[e] Taken from the catalog presented in Hilton et al. (2009) where H09 ID is given; otherwise measured from the Palomar K_s-band data described in Stanford et al. (2006). If no value is given, the object was not detected in either K_s-selected catalog.
[f] ID in the catalog of Hilton et al. (2009).
[g] "✓" indicates that 3727 Å [O II] emission was identified in the object spectrum.

given population than a single Gaussian. For $n = 2$, we found that the sample of 31 galaxies within R_{200} does not favor a bimodal Gaussian distribution ($P = 0.603$), and this remains the case when considering galaxy samples out to larger radius.

We conclude that despite the significantly increased size of the redshift catalog, there is no clear evidence from the velocity distribution that the cluster consists of two kinematically distinct structures. However, the fact that the Hartigan & Hartigan (1985) dip test still mildly favors a bimodal distribution suggests that the cluster may not be completely relaxed.

5. MID-IR OBSERVATIONS

5.1. Data Reduction and Photometry

J2215 was observed at 24 μm using MIPS on 2008 June 21 as part of the same program that obtained the IRAC observations

described in Section 3.1. The angular resolution of MIPS is 6″, which corresponds to a physical scale of 51 kpc at the cluster redshift in our adopted cosmology. A total of 60 frames each of 30 s integration time were obtained using a large field size dither pattern of 15 cycles centered on the cluster. The BCDs as processed by the Spitzer Science Center were corrected for the effects of bright and dark latents, gradients, and the "jailbar" effect using a flat-field calibration generated from the data itself. The calibrated data were then mosaiced together using the MOPEX package (Makovoz & Khan 2005) to produce a final 5.′5 × 6.′3 image at 1.″25 pixelization roughly centered on the cluster position. A significant fraction of the pixels in the top left corner of many of the individual BCD frames were flagged as suffering from soft saturation, amounting to ≈14% of the total data collected. These pixels were rejected in the mosaicing process and are therefore not included in the final science frame. Consequently, the noise level is higher in this region, which is located >2′ away from the cluster position toward the northeast. As a result, the median exposure time in the final mosaic is reduced to ≈1620 s per pixel, although the exposure time over ≈50% of the mosaic, including the cluster center, is ≈1800 s per pixel.

Photometry was performed using the APEX package (Makovoz & Marleau 2005), where we adopt point response function (PRF) fitted fluxes as measurements of the total source flux, since at the cluster redshift the member galaxies are unresolved by MIPS. The PRF model used was estimated from point sources detected at S/N > 10 in an initial pass over the mosaic. We checked that the PRF estimate was of sufficient accuracy by visual inspection of a residual image in which all detected point sources had been subtracted. Our final 24 μm catalog contains a total of 152 sources detected at >5σ.

We checked the flux detection and completeness limits of our 24 μm mosaic using simulations. We inserted 10 artificial point sources, covering a wide range in flux, at random positions in the point-source-subtracted mosaic (which should have the same noise properties as our science mosaic), and attempted to recover them using the same extraction procedure used to make the catalog from the science mosaic. This process was repeated 300 times. We estimate that the 50% completeness limit of our observations is approximately 70 μJy on the basis of these simulations. Using the Dale & Helou (2002) spectral templates, this translates into a corresponding IR luminosity limit of $L_{\rm IR} > 3 \times 10^{11} L_{\odot}$ at the cluster redshift. Assuming the Kennicutt (1998) law, this implies that we will detect cluster members with SFR > 60 $M_{\odot}$ yr^{-1} (see Section 6) at this completeness level. Thus, we are only able to detect starburst galaxies at the cluster redshift.

5.2. Source Matching

We cross-matched the 24 μm catalog against the optical and near-IR catalogs described in Section 3, using a 2″ matching radius (Bai et al. 2007). For some objects, multiple possible counterparts were identified within the matching radius; we adopt the nearest source as the match where this occurs. Matches were found for a total of 118 >5σ 24 μm sources in this process. We estimated the probability of spurious matches by randomizing the positions of all the 24 μm sources in the catalog and repeating the cross-matching procedure. We estimate a 15% ± 3% chance of a given 24 μm source being randomly associated with an optical/near-IR source, following 100 trials.

Our interest is restricted to sources identified as cluster members, and we find that a total of four objects in the spectroscopic redshift catalog (Table 2) are associated with >5σ 24 μm detections. All of these objects show some evidence of [O II] emission in their spectra. We supplement this sample with a further four objects identified as being cluster members through their photometric redshifts (see Hilton et al. 2009, we assume these objects are all at $z = 1.46$). The typical scatter in the photometric redshift residuals ($\delta z = (z_s - z_p)/(1 + z_s)$, where z_s and z_p are the spectroscopic and photometric redshifts respectively) is ≈0.04 (Hilton et al. 2009). Note that one object thought to be a spurious detection has been removed from this sample after visual inspection of all cluster members. None of the objects in this sample have alternative optical/near-IR counterparts within the 2″ matching radius used.

In addition to these objects, we found that there is a very prominent, bright (239 ± 9 μJy) 24 μm source located 17″ away (≈0.15 Mpc at $z = 1.46$) from the cluster center that is not included by the above sample selection criteria. It has an insecure ($Q = 1$) spectroscopic redshift that hints it could be a cluster member, and in addition, is not unambiguously identified with a single optical/near-IR object: an object with a photometric redshift consistent with cluster membership from the H09 catalog is also located within the matching radius. Furthermore, the local environment of this object is somewhat crowded, as Figure 5 shows; there are two other galaxies within $\lesssim$2.″2 that were selected as photometric members of the cluster in the H09 catalog. This suggests that the source is likely to be physically associated with the cluster. We will refer to this object

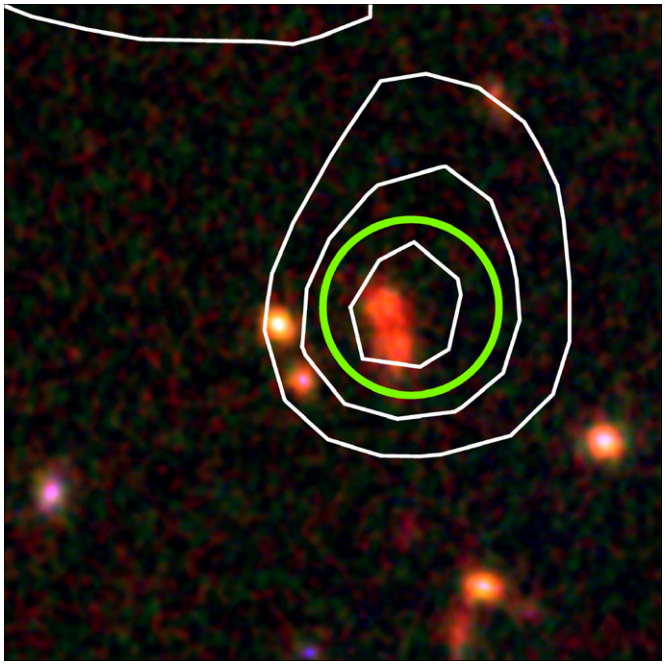

Figure 5. False color image (z_{850}, J, K_s) of a zoomed-in 15″ × 15″ region in the vicinity of a prominent, bright (239 ± 9 μJy) 24 μm source located ≈17″ from the cluster center (SSTU J221559.68−173758.9). North is toward the top of the image and east is toward the left. The contour overlay shows the MIPS 24 μm data. The green circle is centered on the position of the 24 μm source and shows the 2″ radius used in cross-matching the 24 μm catalog to the optical/near-IR catalogs (see Section 5.2). Although the source is not spectroscopically confirmed as a cluster member, the two galaxies within the matching circle have a $Q = 1$ (insecure) spectroscopic redshift and a photometric redshift concordant with the cluster redshift. In addition, the two galaxies to the left of the source, just outside the matching radius, were selected as members in the photometric redshift catalog of Hilton et al. (2009), suggesting that the source is likely to be associated with the cluster.

(A color version of this figure is available in the online journal.)

(SSTU J221559.68−173758.9) as the "unconfirmed source" in the following discussion of the nature of the sources. It is possible that both of the candidate optical/near-IR counterparts of this object contribute to the measured 24 μm flux.

We also cross-matched the MIPS source list against the X-ray point sources identified in our *Chandra* observations (Section 2). We find that none of the 24 μm sources associated with cluster members are X-ray sources. However, one bright 24 μm source with flux density $f_{24} = 820 \pm 10$ μJy (SSTU J221600.14−173836.8) is associated with the *Chandra* source PS3 (see Table 1), which is located only $\approx$0.′7 from the cluster center. As mentioned in Section 2.1, this object is likely to be a high-redshift ($z_p \sim 2.5$) obscured AGN behind the cluster.

6. NATURE OF THE CLUSTER X-RAY AND MID-INFRARED SOURCES

6.1. Infrared Colors

Re-radiation by dust is the source of the 24 μm flux from the cluster mid-IR sources, but this emission can be powered primarily by either star formation or AGN. Studies of both the field (e.g., Pérez-González et al. 2008a) and lower redshift clusters (e.g., Geach et al. 2006; Marcillac et al. 2007) suggest that <10% of the 24 μm emitters are likely to be powered by AGN rather than star formation; here we perform some simple tests to determine the nature of the sources in J2215.

Luminous ($L_{\rm X(2-10\ keV)} \gtrsim 10^{42}$ erg s^{-1}) X-ray point sources are powered by AGN rather than starburst activity (e.g., Georgakakis et al. 2007). As mentioned above (Section 5.2), none of the sample of 24 μm emitting cluster members are associated with X-ray point sources detected in our *Chandra* data, which reaches a limiting flux of $\approx 1.0 \times 10^{-16}$ erg s^{-1} cm^{-2} (roughly corresponding to $L_{\rm X(2-10\ keV)} > 0.8 \times 10^{42}$ erg s^{-1} at the cluster redshift, assuming spectral index $\alpha = 2$ and $N_{\rm H} = 1 \times 10^{22}$ cm^{-2}).

Another way to identify AGNs is through their IR colors (Stern et al. 2005). Figure 6 shows the [3.6]−[4.5], [5.8]−[8.0] color–color plot of the 24 μm emitting cluster members. Unfortunately, the uncertainties on the [5.8]−[8.0] colors are large: the mean error is $\approx$0.6 mag, which limits our ability to draw firm conclusions from this test. This is driven by the fact that only three of the 24 μm sources are detected at $>3\sigma$ in the 8.0 μm channel. One source (SSTU J221558.94−174101.2) is not detected at either 5.8 μm or 8.0 μm. We overplot in this figure the non-evolving tracks of several spectral templates taken from the library of Polletta et al. (2007). The shaded area shows the region of color–color space occupied primarily by broad-lined AGNs according to the criteria of Stern et al. (2005). Figure 6 shows that only one of the cluster 24 μm sources falls within this region (SSTU J221600.38−173750.5). The other 24 μm sources have colors consistent with star-forming galaxies at this redshift.

We also plot the positions of the X-ray point sources identified in the *Chandra* data (Section 2) in Figure 6. The source which is detected in both the X-ray and 24 μm data is very red in [5.8]−[8.0] color, consistent with it being an obscured, high-redshift AGN. Of the two *Chandra* sources that are spectroscopically confirmed cluster members, one lies inside the QSO region of color–color space, whereas the other has similar colors in the IRAC bands to the cluster 24 μm sources. However, as with the 24 μm sources, the color uncertainties are large.

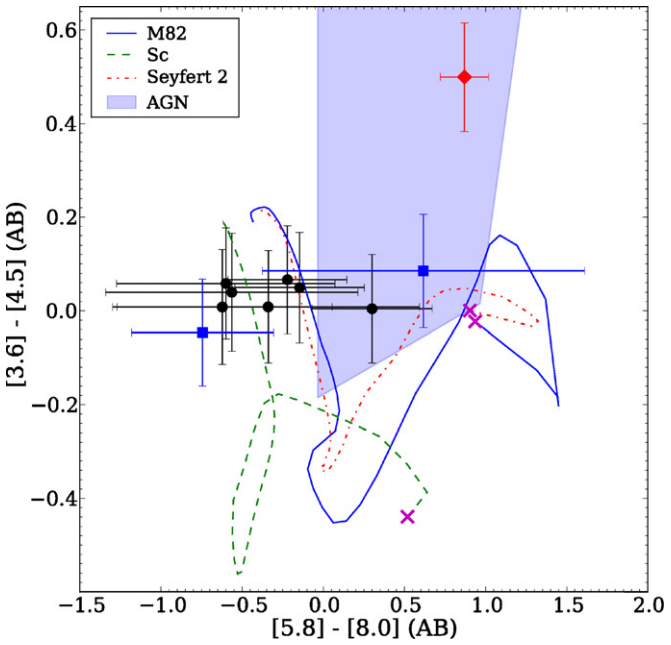

Figure 6. IRAC color–color plot of the 24 μm emitting cluster members (circles). Overplotted are non-evolving tracks of various spectral templates as they are redshifted from $z = 0$ to $z = 2$ (see the legend; the crosses indicate the $z = 0$ end of each track), taken from the library of Polletta et al. (2007). Clearly, the colors of most of the cluster 24 μm sources are not consistent with those expected of Type I QSOs (shown by the shaded area marked "AGN" in the legend), and are more similar to those expected of star-forming galaxies at this redshift. The X-ray/24 μm source (SSTU J221600.14−173836.8; see Section 5.2, marked with a diamond) occupies the same region of the color–color plane as the QSOs. The positions of the X-ray point sources that are not 24 μm sources (PS1 and PS2; see Section 2) are marked with squares.

(A color version of this figure is available in the online journal.)

The IRAC colors do not allow us to distinguish between normal galaxies and narrow-lined AGN such as the Seyfert 2 class, as shown by the template tracks in Figure 6. However, galaxies of this class are often host to significant star-forming activity, generally being dominated by signatures of star formation at optical and IR wavelengths (e.g., Della Ceca et al. 2001; Cid Fernandes et al. 2004; Panessa et al. 2005).

6.2. Star Formation

We now proceed to estimate IR luminosity ($L_{\rm IR}$) derived SFRs for cluster 24 μm sources that were not classified as AGNs due to either their IR colors or the presence of X-ray emission. We include the "unconfirmed source" (SSTU J221559.68−173758.9; Section 5.2 and Figure 5) and the source undetected in the 5.8 μm and 8.0 μm channels (SSTU J221558.94−174101.2) in this sample. We first derive 8–1000 μm luminosities ($L_{\rm IR}$) from the measured 24 μm flux densities using the full range of templates in the libraries of Chary & Elbaz (2001) and Dale & Helou (2002). Throughout this analysis we treat each template library independently. Because we lack the longer wavelength data needed to constrain the spectral energy distributions (SEDs), we take the median $L_{\rm IR}$ value derived from each template set as the best estimate of $L_{\rm IR}$, and adopt the minimum and maximum values of $L_{\rm IR}$ as error bars. These systematic errors dominate over the random error due to uncertainty in the 24 μm flux measurements. The $L_{\rm IR}$ values are then converted into SFRs using the Kennicutt (1998) law. The derived IR luminosities and SFRs for each cluster galaxy in the sample are listed in Table 3.

Table 3
Mid-IR Derived Star Formation Rates for 24 μm Emitting Members of J2215.9−1738

SSTU	Alt. ID[a]	f_{24} (μJy)	CE01 L_{IR} ($\times 10^{11}$ $L_\odot$)	CE01 SFR ($M_\odot$ yr^{-1})	DH02 L_{IR} ($\times 10^{11}$ $L_\odot$)	DH02 SFR ($M_\odot$ yr^{-1})	r (Mpc)
Spectroscopic members							
J221557.24−173753.2	35	159 ± 10	$9.0^{+8.0}_{-2.8}$	160^{+140}_{-50}	$7.7^{+23.8}_{-2.5}$	130^{+410}_{-40}	0.17
J221556.92−173804.7	39	98 ± 9	$5.6^{+4.7}_{-1.7}$	100^{+80}_{-30}	$4.7^{+14.1}_{-1.5}$	80^{+240}_{-30}	0.19
J221600.38−173750.5[b]	53	159 ± 9	$9.0^{+7.9}_{-2.8}$	155^{+135}_{-47}	$7.7^{+23.4}_{-2.5}$	131^{+403}_{-42}	0.25
J221609.88−173826.4	371	93 ± 9	$5.3^{+4.9}_{-1.7}$	90^{+80}_{-30}	$4.5^{+14.3}_{-1.5}$	80^{+250}_{-30}	1.39
J221558.94−174101.2	400	122 ± 12	$7.0^{+6.7}_{-2.2}$	120^{+120}_{-40}	$6.0^{+19.5}_{-2.0}$	100^{+340}_{-30}	1.51
Photometric members							
J221558.22−173822.1	899	108 ± 9	$6.2^{+5.7}_{-1.9}$	110^{+100}_{-30}	$5.2^{+16.6}_{-1.7}$	90^{+290}_{-30}	0.17
J221556.80−173721.9	529	244 ± 10	$13.9^{+12.7}_{-4.3}$	240^{+220}_{-70}	$11.8^{+37.4}_{-3.9}$	200^{+640}_{-70}	0.40
J221554.62−173855.0	1118	73 ± 9	$4.2^{+3.8}_{-1.3}$	70^{+70}_{-20}	$3.5^{+11.2}_{-1.2}$	60^{+190}_{-20}	0.65
Unconfirmed sources							
J221559.68−173758.9	744/747	239 ± 9	$13.7^{+13.1}_{-4.3}$	240^{+230}_{-70}	$11.6^{+38.0}_{-3.8}$	200^{+650}_{-70}	0.15

Notes. Columns labeled CE01 have quantities derived using the Chary & Elbaz (2001) spectral templates; likewise, quantities in columns labeled DH02 are calculated using the Dale & Helou (2002) templates. The minimum and maximum derived IR luminosities from each template library are quoted as error bars on L_{IR} and SFR.

[a] The ID number in this column corresponds to the ID given in Table 2 for objects with spectroscopic redshifts. For objects with photometric redshifts and SSTU J221559.68−173758.9, this ID number corresponds to that in the catalog of Hilton et al. (2009).

[b] This object is more likely to be an AGN rather than a star-forming galaxy, based on its IRAC colors (see Section 6.1).

As Table 3 shows, all of the 24 μm sources in J2215 can be classified as Luminous Infrared Galaxies (LIRGs; galaxies with $L_{IR} > 10^{11}$ $L_\odot$), and have very high SFRs, typically $\sim$100 $M_\odot$ yr^{-1}. If the unconfirmed 24 μm source (Section 5.2 above) is actually a cluster member, it is an Ultra Luminous Infrared Galaxy (ULIRG; $L_{IR} > 10^{12}$ $L_\odot$)—although this luminosity may be overestimated somewhat due to the presence of a neighboring galaxy within $<1''$ (Figure 5). Neglecting the unconfirmed 24 μm source, there are three objects at projected clustercentric radii <250 kpc with very high SFRs, and so intense star formation may be taking place in the heart of the cluster, as also hinted at by the narrow-band [O II] imaging of Hayashi et al. (2010). Studies of the environmental dependence of SFR in the field have shown that SFR actually increases with increasing local galaxy density at $z \sim 1$, whereas the opposite trend is observed in the local universe (Elbaz et al. 2007; Cooper et al. 2008). However, these studies also show that the SFR falls off beyond a critical peak galaxy density. There is $\approx$1.5 Gyr difference in look-back time between the redshift of J2215 and $z = 1$, and so perhaps it is possible that we are seeing the peak of the local density–SFR relation shift to higher densities as redshift increases.

The median values of L_{IR} and SFR that we estimate for each galaxy are consistent between both the template libraries of Chary & Elbaz (2001) and Dale & Helou (2002), although we note that the upper limit of L_{IR} and SFR estimated using the Dale & Helou (2002) templates is significantly higher. It is possible that the lower limit on the values in Table 3 may be overestimated, if neither of the template libraries, which are based on observations at considerably lower redshift, are representative of galaxies at $z \approx 1.5$. Murphy et al. (2009) show that this is likely to be the case from mid-IR spectroscopic observations of galaxies in this redshift regime. In particular, the equivalent widths of features due to polycyclic aromatic hydrocarbons (PAHs) seem to be underestimated by the Chary & Elbaz (2001) templates compared to observed high-redshift galaxies, and for galaxies with $L_{IR} > 3 \times 10^{13}$ $M_\odot$ and $z > 1.4$ this leads to an overestimate of L_{IR} by a factor of $\sim$5 when L_{IR} is derived from 24 μm data alone. For J2215 at $z = 1.46$, a broad PAH feature at 8.6 μm is redshifted into the MIPS 24 μm band, and so this may be an issue for the measurements reported in Table 3. Longer wavelength data (e.g., at 70 μm) are required to investigate this issue further, and it has been shown that such data significantly improves the constraints on L_{IR} inferred from template fitting, particularly at high redshifts (see Figure 2 of Murphy et al. 2009).

Other lower redshift studies have used 24 μm observations to quantify the fraction of star-forming galaxies f_{SF} in clusters, finding f_{SF} to increase from $\approx$3% at $z \approx 0$ to $\approx$13% by $z \approx 0.8$ (e.g., Saintonge et al. 2008; Haines et al. 2009b). Given the depth of our 24 μm observations, and the fact that sample definitions used to estimate f_{SF} vary, we are only able to attempt a very rough estimate of f_{SF} in J2215. We find $f_{SF} \sim 16\%$ for galaxies within R_{200} and brighter than $\approx M^* + 1.5$ in the galaxy luminosity function, using only galaxies with $L_{IR} > 3.3 \times 10^{11}$ $L_\odot$ (i.e., SFR $\gtrsim 60$ $M_\odot$ yr^{-1}) to define the star-forming sample. Note that we exclude the "unconfirmed source" (SSTU J221559.68−173758.9) in making this estimate. The higher cut in L_{IR} used here compared to that used in, e.g., Haines et al. (2009b) to define f_{SF} ($L_{IR} > 5 \times 10^{10}$ $L_\odot$) suggests that the star-forming fraction in J2215 may be even higher, if an equivalent, lower cut in L_{IR} was used.

6.3. Optical Properties

Using the catalog from H09, we can investigate the optical properties of the six 24 μm emitting cluster galaxies within R_{200}, in addition to the objects detected in the *Chandra* X-ray observations. Figure 7 shows the $z_{850}-J$ color–magnitude diagram of the cluster with the 24 μm cluster members highlighted. Three of these galaxies are within $<2.3\sigma$ of the cluster red sequence. Lower redshift studies have also found a significant number of 24 μm emitting, presumably star-forming, cluster members close to the red sequence, and that the contribution of these galaxies to the total star-forming population in clusters increases with redshift (Saintonge et al. 2008). However, the

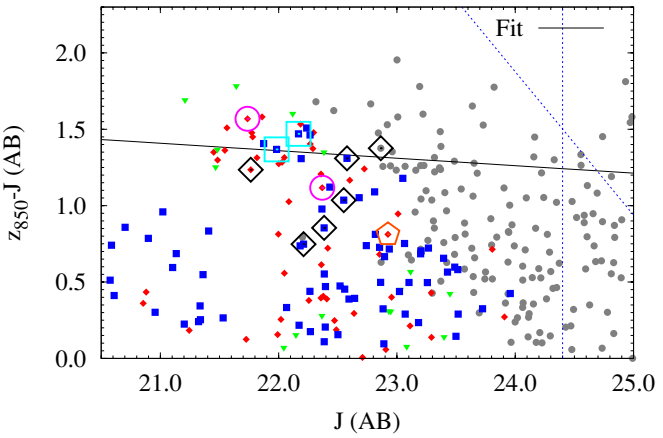

Figure 7. $z_{850}-J$ color–magnitude diagram of all galaxies within 0.8 Mpc of the center of J2215.9−1738. Elliptical galaxies are marked as red diamonds; S0s with green triangles; late-type galaxies with blue squares; and galaxies for which morphologies were not determined with gray circles (see Hilton et al. 2009 for details of the morphological classifications). The 24 μm emitting cluster members are outlined by the large black diamonds; both possible optical counterparts to the unconfirmed 24 μm source (shown in Figure 5) by cyan squares; the X-ray emitting cluster members by the magenta circles; and the 24 μm and X-ray source (likely to be a high-redshift obscured AGN) by the orange pentagon. The solid black line marks the fit to the color–magnitude relation of early-type galaxies within the cluster measured by Hilton et al. (2009). Several of the 24 μm sources lie close to the cluster red sequence, indicating that not all of these galaxies are "red-and-dead."

(A color version of this figure is available in the online journal.)

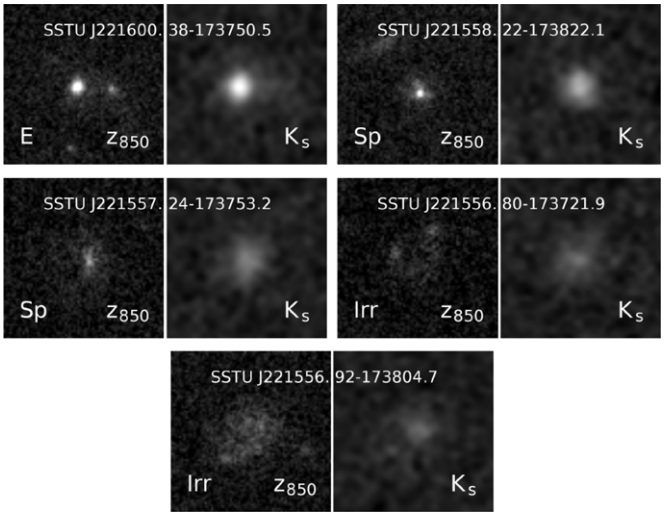

Figure 8. ACS z_{850} and MOIRCS K_s postage stamp images of 24 μm emitting members of J2215.9−1738 that fall within the ACS/MOIRCS imaging area (see Hilton et al. 2009 for details). Each image is 3.″75 on a side. Most of the galaxies are of irregular (Irr) or spiral (Sp) type. Only one of the galaxies is elliptical (and this object is likely to be powered by an AGN based on its IR colors; see Section 6.1), and one galaxy fainter than $z_{850} > 24$ was not morphologically classified.

brightest of these objects in J2215 is likely to be an AGN based on its IR colors (SSTU J221600.38−173750.5, see Section 6.1). This object was also morphologically classified as an elliptical galaxy by H09. All of the other 24 μm sources, which are most likely powered predominantly by star formation, have late-type morphologies (spiral or irregular; see Figure 8).

The two possible optical counterparts to the unconfirmed 24 μm source (SSTU J221559.68−173758.9, Figure 5) are highlighted in Figure 7. These objects are both slightly redder than the cluster red sequence, but lie within $<1\sigma$ of it, and were morphologically classified as late-type galaxies by H09. If this source is truly within the cluster, it is therefore likely to be an example of a red-sequence galaxy with a high SFR.

We also plot the positions of the X-ray sources in Figure 7. The cluster member X-ray sources (PS1 and PS2; Section 2) are both within $<2\sigma$ of the red sequence, whereas the high-redshift, obscured QSO in the background of the cluster is considerably bluer than the red sequence.

6.4. Stellar Population Modeling and Specific Star Formation Rates

We investigated the stellar populations of the 24 μm sources located within R_{200} by fitting their broadband SEDs to the models of Bruzual & Charlot (2003). We combined the IRAC photometry (Section 3.1) with the rest-frame optical photometry presented in H09, using the `SExtractor` `MAG_AUTO` magnitudes in the latter case as estimates of total magnitude. Note that the cross-matching between the IRAC and the K_s selected catalog described in Section 3.1 showed that each of the six 24 μm sources is uniquely associated with a single corresponding object across both catalogs. However, the IRAC photometry for one object (SSTU J221558.22−173822.1) suffers from blending with another galaxy $\approx$2.″2 away. The blended galaxy is $\approx$1 mag fainter at K_s, and so we expect that this should lead to only a small overestimate of the stellar mass of this object.

We followed a similar approach to Shapley et al. (2005) in performing the SED fitting. We use a grid of solar metallicity models with exponentially declining star formation histories with 20 values of τ in the range 0.1–20 Gyr, and 50 ages in range 0.001–4 Gyr, i.e., constrained such that the maximum allowed age is less than that of the universe at $z = 1.46$. We adopt a Chabrier (2003) initial mass function (IMF). We include the effect of dust extinction using the Calzetti et al. (2000) law, allowing the value of $E(B-V)$ to vary between 0.0 and 0.5 in steps of 0.02. We fitted the SEDs by analytically calculating the normalization N for each model SED where $d\chi^2/dN = 0$, adopting the model with the lowest χ^2 value as the best fit. The stellar mass M_* is then estimated from the value of N. We therefore fit for a total of four parameters (age, τ, $E(B-V)$, and M_*).

We estimated the errors on parameters through Monte Carlo simulations; we generated 1000 fake SEDs for each object by replacing each flux measurement with a random variate drawn from a Gaussian distribution consistent with the observed photometric uncertainties, and fitted them using the same method used for the real data as described above. We adopt 68.3 percentile confidence intervals as our error estimates, measured as the corresponding fraction of the fits to the Monte Carlo realizations.

Figure 9 shows the results. The SEDs of the 24 μm emitting cluster members are in most cases best fit by young (age $<$ 400 Myr) stellar populations, with large dust extinction values ($E(B-V) > 0.2$). However, there are many degeneracies between the fitted parameters (such as between τ and $E(B-V)$; see the discussion in, e.g., Shapley et al. 2005) and different stellar population models yield systematically different results; for example, if we instead fit the SEDs using the Maraston (2005) models, we generally obtain higher $E(B-V)$ values and younger ages. We note that in most cases the reduced χ^2 values indicate that the fits are not especially good. The worst case (J221600.38−173750.5 with $\chi^2/\nu = 10.6$) was classified

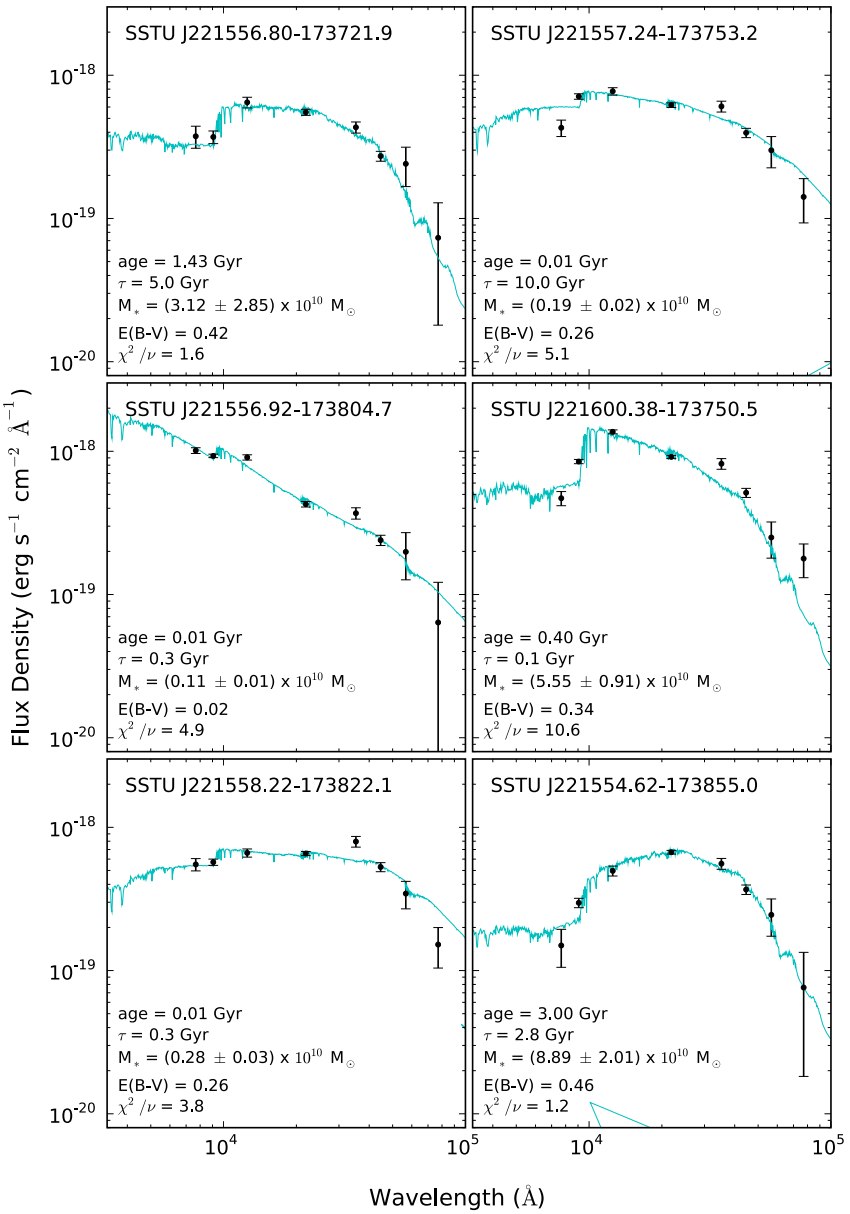

Figure 9. Broadband SEDs of the six 24 μm emitting cluster members with available rest-frame optical photometry from Hilton et al. (2009) and IRAC photometry from this work (points). The best-fitting Bruzual & Charlot (2003) model is shown by the solid line. Note that the object with the highest χ^2/ν value (J221600.38−173750.5) is likely to host an AGN based on its IR colors (Section 6.1).

(A color version of this figure is available in the online journal.)

as an AGN based on its IR colors (see Section 6.1), and so the poor fit for this object is not surprising.

A number of authors have found that SED-based stellar mass estimates are reasonably robust, despite degeneracies between other stellar population parameters (e.g., Shapley et al. 2005; Muzzin et al. 2009). We used the stellar mass measurements derived from the SED fitting to estimate specific star formation rates (SSFRs) for the cluster 24 μm sources. Figure 10 shows the results. Despite the very small sample size, we recover the well-known result that the lowest mass galaxies are building up their stellar mass most rapidly, having the highest SSFRs. The cluster 24 μm sources follow a similar SSFR–M_* relation to that measured in the field at $1.0 < z < 1.5$ (e.g., Santini et al. 2009), although the SSFRs of the cluster sources appear to be biased high compared to the field sample. However, the field galaxy sample contains relatively fewer objects at $z \sim 1.5$ compared to the low end of the sample redshift range, and the locus of the relation moves upward in Figure 10 as redshift increases. It is also possible that the cluster galaxy SFRs, which are derived from the 24 μm fluxes alone, may be overestimated (see the discussion in Section 6.2).

7. DISCUSSION

7.1. The Impact of Unresolved Point Sources on High-redshift X-ray Cluster Surveys

As the results of this paper show, the presence of emission from unresolved point sources in X-ray observations of high-redshift clusters of galaxies can lead to significant biases in temperature measurements if unaccounted for. As cosmological analyses of X-ray cluster surveys rely on temperature as a mass proxy, the increase in the X-ray AGN population with redshift

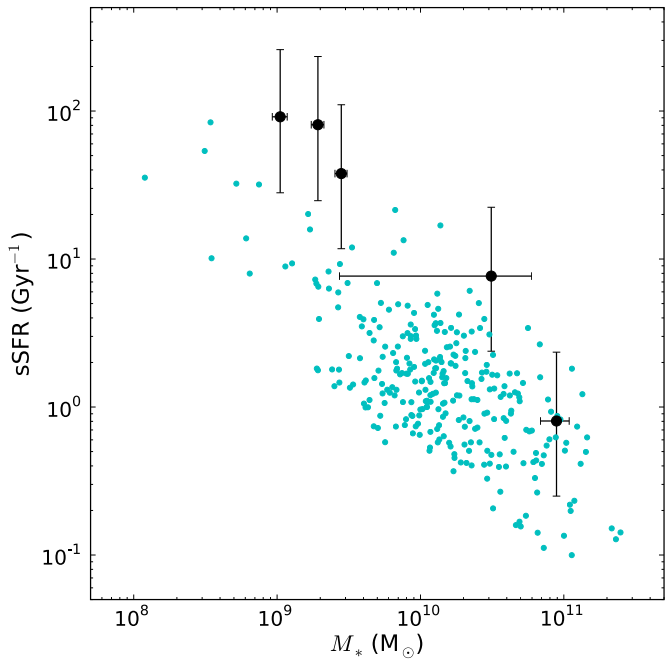

Figure 10. SSFR vs. stellar mass (M_*) for the five 24 μm emitting cluster members not classified as AGN plotted in Figure 9 (large points with error bars). The data from the $1.0 < z < 1.5$ field sample of Santini et al. (2009) are also plotted for comparison (small points). Note that the values for the field sample have been scaled to a Chabrier (2003) IMF, as was used in deriving the values for the cluster galaxies. The 24 μm emitting cluster galaxies appear to follow a similar SSFR–M_* relation to field galaxies at this redshift, though the error bars are large. The SFRs for the cluster galaxies, estimated from the 24 μm fluxes alone, may be overestimated (see the discussion in Section 6.2).

(A color version of this figure is available in the online journal.)

is therefore likely to also bias any cosmological interpretation that includes such high-redshift objects. This issue is not likely to affect XCS, as it is planned to exclude $z > 1$ clusters from the cosmological analysis, as few such systems will be detected (Sahlén et al. 2009). However, this may be an issue for larger scale, low-resolution X-ray surveys such as the upcoming all-sky *eROSITA* mission (Predehl et al. 2010), which will detect tens of thousands of galaxy clusters out to $z \approx 1.3$, including ∼500 at $z > 1$. To extract the full cosmological information from this sample will therefore require either a follow-up program of high-resolution pointed observations of detected high-redshift clusters, or could alternatively perhaps be addressed statistically, using the existing data in the *Chandra* archive to derive the amount of contamination by AGN in clusters as a function of redshift (e.g., Martini et al. 2009; Gilmour et al. 2009).

7.2. Star Formation in High-redshift Galaxy Clusters

The results of our analysis suggest that the core of J2215 may contain galaxies with very high SFRs, as 24 μm sources which are likely to be powered by star formation are found within projected distances of <250 kpc of the cluster X-ray position. Significant star-forming activity in the cluster core is also suggested by the narrow-band [O II] observations by Hayashi et al. (2010), which are sensitive to galaxies with lower SFRs (>2.6 $M_\odot$ yr^{-1}) than is probed by our MIPS observations.

Studies of clusters at lower redshift have revealed a significant amount of obscured star formation in clusters; however, this activity seems to take place mostly in the infall regions, and not in the cluster cores (Geach et al. 2006; Marcillac et al. 2007; Saintonge et al. 2008; Haines et al. 2009b; Koyama et al. 2010). This suggests that triggered star formation, driven by the interaction of infalling galaxies with the cluster potential, is one of the main channels for transforming star-forming, late-type galaxies in clusters into passively evolving early-type galaxies. In this scenario, the gas within infalling galaxies is compressed upon entering the cluster, leading to a burst of star formation which rapidly uses up the available gas reservoir, eventually leading to star formation being quenched. If this is the general case, then why are high SFRs observed in the center of J2215?

Perhaps environmental differences between clusters are responsible, as the amount of star formation in clusters is seen to vary significantly from cluster to cluster (e.g., Geach et al. 2006). At low redshift, there are hints that the dynamical state of the cluster plays a role. Braglia et al. (2009) examined star formation in two $z \approx 0.3$ clusters of opposite dynamical state: one of their targets was a relaxed, cool core cluster, while the other appears to be a merger. They found a significantly increased fraction of star-forming galaxies within R_{200} in this latter system. Similarly, Haines et al. (2009a) examined star formation in the merging system A1758 at $z = 0.28$, finding significant dust obscured star formation taking place within <500 kpc of the core of one of the components of this system, suggesting that cluster mergers can trigger star formation in cluster galaxies.

Although J2215 is not resolved into two kinematically distinct components with the current spectroscopic sample of members (Section 4.3), the limited data currently available hints that the cluster may be dynamically somewhat disturbed. In addition to the cluster velocity distribution, the cluster lacks an obvious BCG, and the BCG candidate selected in the study by Collins et al. (2009) is located at a significant offset of ≈300 kpc from the cluster X-ray position.

It will be interesting to compare our results for J2215 to the properties of star-forming galaxies in the few other $z > 1.3$ clusters that are currently known (Mullis et al. 2005; Stanford et al. 2005; Eisenhardt et al. 2008; Wilson et al. 2009; Papovich et al. 2010; Tanaka et al. 2010). In particular, XMMU J2235.3−2557 at $z = 1.39$ (Mullis et al. 2005) appears to be a very relaxed and mature system already at this epoch, showing evidence of a cool core X-ray morphology (Rosati et al. 2009), and the core of this cluster is dominated by a group of massive, passively evolving galaxies, the brightest of which are significantly brighter than the BCG in J2215 (Lidman et al. 2008; Hilton et al. 2009). Furthermore, this cluster appears to be ≈3 times more massive than J2215 based on a comparison of the cluster X-ray temperatures (Rosati et al. 2009; Jee et al. 2009), and may therefore be expected to have a lower fraction of star-forming galaxies than J2215 if star formation is truncated earlier in more massive systems.

8. CONCLUSIONS

We have explored the AGN and star-forming populations of the cluster J2215.9−1738 at $z = 1.46$ using high-resolution X-ray data from the *Chandra* satellite and IR observations from the *Spitzer Space Telescope*. This is the first study of star formation as traced by mid-IR observations in a cluster at $z \approx 1.5$. We found the following.

1. The cluster emission is contaminated by X-ray point sources, leading to the X-ray temperature being overestimated in the analysis presented in S06; however, these point sources only contribute ≈15% to the total flux. Two of the X-ray point sources revealed by the *Chandra* observations

are cluster members, while a third has properties consistent with it being a high-redshift, highly obscured AGN in the background. The cluster has temperature $T = 4.1^{+0.6}_{-0.9}$ keV and bolometric luminosity $L_X = (2.92^{+0.24}_{-0.35}) \times 10^{44}$ erg s^{-1} (extrapolated to 2 Mpc radius) from a joint analysis of the *XMM-Newton* and *Chandra* data. The cluster is less luminous than expected from self similar evolution of the local L_X–T relation at the $\approx 2\sigma$ level.

2. The velocity dispersion of the cluster is measured to be $\sigma_v = 720 \pm 110$ km s^{-1}, from 31 galaxies within R_{200}. There is no clear evidence that the cluster velocity distribution is composed of two kinematically distinct components, although the Hartigan & Hartigan (1985) dip test of unimodality still hints that the cluster is not completely relaxed. Following the revised X-ray analysis presented in this paper, the cluster is found to lie on the σ_v–T relation, contrary to the result reported in H07.
3. Mid-IR imaging reveals a total of eight $>5\sigma$ 24 μm sources that are cluster members, selected using spectroscopic or photometric redshifts. In addition, there is a prominent 24 μm source (J221559.68−173758.9) with two possible optical/near-IR counterparts located $\approx 17''$ from the cluster center that may be associated with the cluster. One of the 24 μm sources is found to have the IR colors expected of an AGN, and has an elliptical morphology. The remaining objects are most likely powered by star formation, and if this is the case have SFRs $\sim 100\, M_\odot$ yr^{-1}, adopting the Chary & Elbaz (2001) spectral templates and assuming that the Kennicutt (1998) law holds at this redshift.
4. The cluster member AGNs identified in the X-ray and IR observations are located within $\lesssim 2\sigma$ of the cluster red sequence, as are three (possibly four) 24 μm sources assumed to be powered by star formation. Three of the 24 μm sources are also found within a projected distance of <250 kpc from the cluster center, suggesting that the core of J2215 may be host to galaxies with very high SFRs, in contrast to clusters at lower redshift.

We thank the referee for a number of suggestions that improved the clarity of this paper. We thank Paola Santini for providing the field galaxy data plotted in Figure 10. This work is based in part on observations with the *Spitzer Space Telescope*, which is operated by the Jet Propulsion Laboratory, California Institute of Technology, under NASA contract 1407, and on observations with the *Chandra X-ray Observatory*. The W. M. Keck Observatory is a scientific partnership between the University of California and the California Institute of Technology, made possible by a generous gift of the W. M. Keck Foundation. Based in part on observations obtained at the Gemini Observatory (program ID GS-2009B-Q-34), which is operated by the Association of Universities for Research in Astronomy, Inc., under a cooperative agreement with the NSF on behalf of the Gemini partnership: the National Science Foundation (United States), the Science and Technology Facilities Council (United Kingdom), the National Research Council (Canada), CONICYT (Chile), the Australian Research Council (Australia), Ministrio da Cincia e Tecnologia (Brazil), and Ministerio de Ciencia, Tecnologa e Innovacin Productiva (Argentina). The analysis pipeline used to reduce the DEIMOS data was developed at UC Berkeley with support from NSF grant AST-0071048. M.H. acknowledges the support of a postdoctoral research fellowship from the University of KwaZulu-Natal. N.M., A.K.R., and E.L.-D. acknowledge financial support from STFC. M.S. acknowledges financial support from the Swedish Research Council (VR) through the Oskar Klein Centre. P.T.P.V. acknowledges the support of POCI2010 through the project POCTI/CTE-AST/58888/2004. This work was performed under the auspices of the U.S. Department of Energy, National Nuclear Security Administration by the University of California, Lawrence Livermore National Laboratory under contract No. W-7405-Eng-48. The authors recognize and acknowledge the very significant cultural role and reverence that the summit of Mauna Kea has always had within the indigenous Hawaiian community; we are fortunate to have the opportunity to conduct observations from this mountain.

REFERENCES

Arnaud, K. A. 1996, in ASP Conf. Ser. 101, Astronomical Data Analysis Software and Systems V, ed. G. H. Jacoby & J. Barnes (San Francisco, CA: ASP), 17
Ashman, K. M., Bird, C. M., & Zepf, S. E. 1994, AJ, 108, 2348
Assef, R. J., et al. 2010, ApJ, submitted (arXiv:1001.4529)
Bai, L., et al. 2007, ApJ, 664, 181
Balogh, M., et al. 2004, MNRAS, 348, 1355
Barmby, P., Huang, J., Ashby, M. L. N., Eisenhardt, P. R. M., Fazio, G. G., Willner, S. P., & Wright, E. L. 2008, ApJS, 177, 431
Beers, T. C., Flynn, K., & Gebhardt, K. 1990, AJ, 100, 32
Bertin, E., & Arnouts, S. 1996, A&AS, 117, 393
Blakeslee, J. P., et al. 2003, ApJ, 596, L143
Bouwens, R. J., et al. 2009, ApJ, 705, 936
Bower, R. G., Benson, A. J., Malbon, R., Helly, J. C., Frenk, C. S., Baugh, C. M., Cole, S., & Lacey, C. G. 2006, MNRAS, 370, 645
Braglia, F. G., Pierini, D., Biviano, A., & Böhringer, H. 2009, A&A, 500, 947
Bruzual, G., & Charlot, S. 2003, MNRAS, 344, 1000
Butcher, H., & Oemler, A., Jr. 1984, ApJ, 285, 426
Calzetti, D., Armus, L., Bohlin, R. C., Kinney, A. L., Koornneef, J., & Storchi-Bergmann, T. 2000, ApJ, 533, 682
Chabrier, G. 2003, PASP, 115, 763
Chary, R., & Elbaz, D. 2001, ApJ, 556, 562
Cid Fernandes, R., Gu, Q., Melnick, J., Terlevich, E., Terlevich, R., Kunth, D., Rodrigues Lacerda, R., & Joguet, B. 2004, MNRAS, 355, 273
Collins, C. A., et al. 2009, Nature, 458, 603
Cooper, M. C., et al. 2008, MNRAS, 383, 1058
Croton, D. J., et al. 2006, MNRAS, 365, 11
Dale, D. A., & Helou, G. 2002, ApJ, 576, 159
Danese, L., de Zotti, G., & di Tullio, G. 1980, A&A, 82, 322
Davis, M., et al. 2003, Proc. SPIE, 4834, 161
Dawson, K. S., et al. 2009, AJ, 138, 1271
Della Ceca, R., Pellegrini, S., Bassani, L., Beckmann, V., Cappi, M., Palumbo, G. G. C., Trinchieri, G., & Wolter, A. 2001, A&A, 375, 781
De Lucia, G., et al. 2006, MNRAS, 366, 499
Dietrich, J. P., Erben, T., Lamer, G., Schneider, P., Schwope, A., Hartlap, J., & Maturi, M. 2007, A&A, 470, 821
Dietrich, J. P., et al. 2006, A&A, 449, 837
Eisenhardt, P. R. M., et al. 2008, ApJ, 684, 905
Eisenstein, D. J., et al. 2003, ApJ, 585, 694
Elbaz, D., et al. 2007, A&A, 468, 33
Ellingson, E., Lin, H., Yee, H. K. C., & Carlberg, R. G. 2001, ApJ, 547, 609
Faber, S. M., et al. 2003, Proc. SPIE, 4841, 1657
Fazio, G. G., et al. 2004, ApJS, 154, 10
Ferrarese, L., & Merritt, D. 2000, ApJ, 539, L9
Galametz, A., et al. 2009, ApJ, 694, 1309
Geach, J. E., et al. 2006, ApJ, 649, 661
Gebhardt, K., et al. 2000, ApJ, 539, L13
Georgakakis, A., Rowan-Robinson, M., Babbedge, T. S. R., & Georgantopoulos, I. 2007, MNRAS, 377, 203
Gilmour, R., Best, P., & Almaini, O. 2009, MNRAS, 392, 1509
Glazebrook, K., & Bland-Hawthorn, J. 2001, PASP, 113, 197
Granato, G. L., De Zotti, G., Silva, L., Bressan, A., & Danese, L. 2004, ApJ, 600, 580
Haines, C. P., Smith, G. P., Egami, E., Okabe, N., Takada, M., Ellis, R. S., Moran, S. M., & Umetsu, K. 2009a, MNRAS, 396, 1297
Haines, C. P., et al. 2009b, ApJ, 704, 126
Hartigan, J. A., & Hartigan, P. M. 1985, Ann. Stat., 13, 70

Hayashi, M., Kodama, T., Koyama, Y., Tanaka, I., Shimasaku, K., & Okamura, S. 2010, MNRAS, 402, 1980
Heckman, T. M. 1980, A&A, 87, 152
Hilton, M., et al. 2007, ApJ, 670, 1000
Hilton, M., et al. 2009, ApJ, 697, 436
Hook, I., et al. 2003, Proc. SPIE, 4841, 1645
Hopkins, P. F., Cox, T. J., Kereš, D., & Hernquist, L. 2008, ApJS, 175, 390
Jee, M. J., et al. 2009, ApJ, 704, 672
Kennicutt, R. C., Jr. 1998, ARA&A, 36, 189
Koyama, Y., Kodama, T., Shimasaku, K., Hayashi, M., Okamura, S., Tanaka, I., & Tokoku, C. 2010, MNRAS, 403, 1611
Kurtz, M. J., & Mink, D. J. 1998, PASP, 110, 934
Lemaux, B. C., Lubin, L. M., Shapley, A. E., Kocevski, D. D., Gal, R. R., & Squires, G. K. 2010, ApJ, 716, 970
Lewis, I., et al. 2002, MNRAS, 334, 673
Lidman, C., et al. 2008, A&A, 489, 981
Magnelli, B., Elbaz, D., Chary, R. R., Dickinson, M., Le Borgne, D., Frayer, D. T., & Willmer, C. N. A. 2009, A&A, 496, 57
Makovoz, D., & Khan, I. 2005, in ASP Conf. Ser. 347, Astronomical Data Analysis Software and Systems XIV, ed. P. Shopbell, M. Britton, & R. Ebert (San Francisco, CA: ASP), 81
Makovoz, D., & Marleau, F. R. 2005, PASP, 117, 1113
Maraston, C. 2005, MNRAS, 362, 799
Marcillac, D., Rigby, J. R., Rieke, G. H., & Kelly, D. M. 2007, ApJ, 654, 825
Markevitch, M. 1998, ApJ, 504, 27
Martini, P., Sivakoff, G. R., & Mulchaey, J. S. 2009, ApJ, 701, 66
Maughan, B. J., Jones, L. R., Ebeling, H., & Scharf, C. 2006, MNRAS, 365, 509
Mei, S., et al. 2009, ApJ, 690, 42
Mullis, C. R., et al. 2005, ApJ, 623, L85
Murphy, E. J., Chary, R.-R., Alexander, D. M., Dickinson, M., Magnelli, B., Morrison, G., Pope, A., & Teplitz, H. I. 2009, ApJ, 698, 1380
Muzzin, A., Marchesini, D., van Dokkum, P. G., Labbé, I., Kriek, M., & Franx, M. 2009, ApJ, 701, 1839
Oke, J. B. 1974, ApJS, 27, 21
Panessa, F., Wolter, A., Pellegrini, S., Fruscione, A., Bassani, L., Della Ceca, R., Palumbo, G. G. C., & Trinchieri, G. 2005, ApJ, 631, 707
Papovich, C., et al. 2006, ApJ, 640, 92
Papovich, C., et al. 2010, ApJ, in press (arXiv:1002.3158)
Pérez-González, P. G., Trujillo, I., Barro, G., Gallego, J., Zamorano, J., & Conselice, C. J. 2008a, ApJ, 687, 50
Pérez-González, P. G., et al. 2008b, ApJ, 675, 234
Polletta, M., et al. 2007, ApJ, 663, 81
Predehl, P., et al. 2010, in AIP Conf. Proc. 1248, X-ray Astronomy 2009: Present Status, Multi-Wavelength Approach, and Future Perspectives, ed. A. Comastri, M. Cappi, & L. Angelini, in press (arXiv:1001.2502)
Romer, A. K., Viana, P. T. P., Liddle, A. R., & Mann, R. G. 2001, ApJ, 547, 594
Rosati, P., et al. 2009, A&A, 508, 583
Sahlén, M., et al. 2009, MNRAS, 397, 577
Saintonge, A., Tran, K.-V. H., & Holden, B. P. 2008, ApJ, 685, L113
Santini, P., et al. 2009, A&A, 504, 751
Seymour, N., et al. 2008, MNRAS, 386, 1695
Shapley, A. E., Steidel, C. C., Erb, D. K., Reddy, N. A., Adelberger, K. L., Pettini, M., Barmby, P., & Huang, J. 2005, ApJ, 626, 698
Silverman, J. D., et al. 2005, ApJ, 624, 630
Smith, G. P., et al. 2005, ApJ, 620, 78
Somerville, R. S., Hopkins, P. F., Cox, T. J., Robertson, B. E., & Hernquist, L. 2008, MNRAS, 391, 481
Stanford, S. A., et al. 2005, ApJ, 634, L129
Stanford, S. A., et al. 2006, ApJ, 646, L13
Stern, D., et al. 2005, ApJ, 631, 163
Tanaka, M., Finoguenov, A., & Ueda, Y. 2010, ApJ, 716, L152
van Dokkum, P. G., et al. 2000, ApJ, 541, 95
Voit, G. M. 2005, Rev. Mod. Phys., 77, 207
Voit, G. M., & Ponman, T. J. 2003, ApJ, 594, L75
Wilson, G., et al. 2009, ApJ, 698, 1943
Yan, R., Newman, J. A., Faber, S. M., Konidaris, N., Koo, D., & Davis, M. 2006, ApJ, 648, 281